Distinct anharmonic characteristics of phonons driven lattice thermal conductivity and thermal expansion in bulk MoSe2 and WSe2

Distinct anharmonic characteristics of phonons driven lattice thermal conductivity and thermal expansion in bulk MoSe$_2$ and WSe$_2$

Mayanak K Gupta[1,2*], Sajan Kumar[1,2], Ranjan Mittal[1,2#], Sanjay K Mishra[1,2], Stephane Rols[3], Olivier Delaire[4], Arumugum Thamizhavel[5], P U Sastry[1,2], and Samrath L Chaplot[1,2]

[1]*Solid State Physics Division, Bhabha Atomic Research Centre, Trombay, Mumbai 400085, India*
[2]*Homi Bhabha National Institute, Anushaktinagar, Mumbai 400094, India*
[3]*Institut Laue-Langevin, BP 156, 38042 Grenoble Cedex 9, France*
[4]*Department of Mechanical Engineering and Materials Science, Duke University, NC 27708, USA*
[5]*Tata Institute of Fundamental Research, Homi Bhabha Road, Colaba, Mumbai 400005, India*
Email: *mayankg@barc.gov.in, [#]rmittal@barc.gov.in*

Using inelastic neutron scattering and X-ray diffraction measurements, together with ab-initio and machine-learned molecular dynamics simulations, we bring out the distinct nature of anharmonicity in the phonon spectra of MoSe$_2$ and WSe$_2$ relevant to thermal transport and thermal expansion behaviour. We show that the perturbation method, including 4th-order force constants, is insufficient to capture the temperature-dependent explicit anharmonicity. The Green-Kubo method captures the explicit anharmonicity and reproduces the thermal conductivity (κ_l) with high fidelity. Our mode-resolved calculation reveals that the major contribution ($\sim 90\%$) to κ_l is attributed to a small explicit anharmonicity of low-energy phonons. In contrast, these modes exhibit large positive Grüneisen parameters (implicit anharmonicity), causing the large thermal expansion of the material.

INTRODUCTION

Low dimensional materials such as transition-metal dichalcogenide (TMDCs) are known to exhibit interesting electronic, optical and thermodynamic properties and are promising materials for applications across thermoelectrics, transistors, optoelectronics, topological materials, solid lubrication, electrode materials for Mg and Zn batteries, energy storage and photovoltaic devices [1-16]. Many TMDCs, such as WSe_2, WS_2, $MoSe_2$ and MoS_2, are considered promising candidates for thermoelectric applications, and comprehensive studies investigated their electronic, optical and transport properties[2-6, 17, 18]. In particular, WSe_2 has been found to exhibit ultralow thermal conductivity in single-layer form[19]. These 2D materials are also promising candidates for flexible electronic devices and nano-electromechanical systems due to their ultralow weight, flexibility and high tensile strength [7, 8, 20-22].

Limited experimental and theoretical studies exist on the thermal conductivity of TMDCs, and they show discrepancies between different measurements and simulations[10, 23-26]. P Jiang et al. measured the anisotropic thermal conductivity on MX_2 (M=Mo, W, X=S, Se) using the time-domain thermoreflectance technique, from which they obtained in-plane (out-of-plane) conductivities ~ 35 W/m-K (2.5 W/m-K)) and 40 W/m-K (2.2 W/m-K), in $MoSe_2$ and WSe_2, respectively, at room temperature[23]. S Kumar et al. used first-principles calculations and found that the three lowest optical modes for bulk $MoSe_2$ and WSe_2 contribute to the lattice thermal conductivity almost as much as the acoustic modes [10]. The authors reported in-plane (out-of-plane) thermal conductivity values at room temperature of ~57 W/m-K (~6 W/m-K), and ~48 W/m-K (~6 W/m-K), for $MoSe_2$ and WSe_2, respectively[10]. Another theoretical investigation of thermal conductivity by Lindroth et al. on WSe_2 and $MoSe_2$ found in-plane and out-of-plane conductivities ~ 33 W/m-K and 4 W/m-K, respectively, for both compounds[24]. These calculations were done with boundary scattering contribution considering a sample size of ~ 1 μm. There are many other TMDCs, for which the thermal conductivity measurements and simulations show significant variance in their values [23, 25-30]. Hence, a comprehensive theoretical study exploring different techniques is informative to clarify the underlying physics of the thermal conductivity in these TMDCs and the possible source of error/variance.

Besides the specifics of TMDCs, a microscopic understanding of thermal properties is generally important to design materials in applications. The anharmonic characteristics of phonons are crucial in both thermal transport and thermal expansion behaviour[31, 32]. For instance, the Grüneisen parameters, which estimate phonon energy shifts due to anharmonicity upon expanding volume, are needed to account for thermal expansivity, while the phonon lifetimes, reflecting anharmonic phonon interactions control

thermal conductivity [33]. Hence, predicting these quantities accurately and rationalizing their microscopic origins can help design materials with tailored properties. Several methods are widely used to compute the lattice thermal conductivity of solids: solving the phonon Boltzmann transport equation (BTE) within perturbation theory[34-36], computing the heat-flux auto-correlation function with equilibrium molecular dynamics[37], or computing the thermal gradient or heat flow using non-equilibrium molecular dynamics[38-40], homogeneous non-equilibrium molecular dynamics[41, 42], atomic green function methods [43, 44], etc. While the perturbation and Green-Kubo methods are among the most popular approaches, all these techniques have certain limitations and advantages.

The lowest-order perturbation theory of the linearized phonon BTE uses the second and third-order force-constants computed around an equilibrium configuration (at T=0 K) and treats finite temperatures by considering the respective phonon occupation numbers. An extension of this method consists in using renormalized second and third-order force-constants at finite temperature, as obtained from ab-initio molecular dynamics (AIMD) simulations, which can extend accuracy to a broader temperature range. However, even at low-T, these methods do not perform well for strongly anharmonic solids where high-order interactions are sizeable. Classical molecular dynamics simulations intrinsically capture all orders of anharmonicity in the interatomic potential, but do not capture the quantum effect at low temperatures. Hence, this approach tends to work best in moderate and high-temperature regimes.

In this manuscript, we calculated the thermal conductivity in $MoSe_2$ and WSe_2 from different techniques. We find that the perturbation methods are not satisfactory, and the machine-learned molecular dynamics (MLMD) simulations quantitatively well capture the higher-order anharmonicity. In addition, we measured the temperature dependence of the phonon density of states (DOS) from 313 K to 1098 K using inelastic neutron scattering (INS), which is used to benchmark our simulations and assess the strength of the anharmonicity. Further, we also measured the thermal expansion by X-ray diffraction (XRD) and calculated the same within the quasi-harmonic approximation (QHA). By combining the experiments and simulations, we found that the contribution of the low-energy (low-E) phonons dominates the heat transport as well as the thermal expansion. These low-E phonons show the right magnitude of the phonon lifetimes and the Gruneisen parameters, which quantitatively reproduce the experimental thermal properties. The details about the sample synthesis, INS and XRD measurements, and state-of-the-art computational techniques of the temperature-dependent effective potential (TDEP) and MLMD are given in supplementary Materials[45].

EXPERIMENTAL

Polycrystalline $MoSe_2$ sample has been prepared from a stoichiometric ratio of high purity Mo (in powder form) and Se in small shots. To start with, the Mo powders and selenium shots were thoroughly ground in an agate mortar. The mixed powders were then cold-pressed into pellets. The pellets were then sealed under a 10^{-6} mbar vacuum in a quartz ampoule. The quartz ampoule was then loaded into a resistive heating box-type furnace. The temperature of the furnace was gradually raised at the rate of 15 ˚C/h up to 900 ˚C and kept at this temperature for about 48 h. Then, the furnace was cooled at a rate of about 20 Deg ˚C/h down to room temperature. We purchased the WSe_2 polycrystalline sample from Sigma Aldrich. Powder XRD was performed to characterize the samples and their phase purity. Temperature-dependent X-ray diffraction studies were carried out using 18 kW rotating Cu anode-based powder diffractometer operating in the Bragg–Brentano focusing geometry with a curved crystal monochromator. Data were collected in the continuous scan mode at a scan speed of $1^{\square}$/minute and step interval of 0.02 degree.

The inelastic neutron scattering measurements were carried out using the high-flux time-of-flight (IN4C) spectrometer at the Institut Laue Langevin (ILL), France, covering a wide range of scattering angles from 10° to 110°. Thermal neutrons of wavelength 2.4 Å (14.2 meV) were used for the measurements. The orientation-averaged scattering function, $S(Q, E)$, was measured in the neutron energy gain mode with momentum transfer, Q, extending up to 7 Å^{-1}. The polycrystalline samples were loaded in a cylindrical niobium sample holder and mounted in a furnace. INS data were collected with samples heated to 313 K, 498 K, 673 and 898 K. The neutron-weighted phonon DOS, $g^{(n)}(E)$ was extracted from the measured $S(Q, E)$ using the incoherent one-phonon approximation as follows

$$g^n(E) = A < \frac{e^{2W(Q)}}{Q^2} \frac{E}{n(E,\ T) + \frac{1}{2} \pm \frac{1}{2}} S(Q, E) > \qquad (1)$$

where A is a normalization constant, and $2W(Q)$ is the Debye-Waller factor. The multiphonon contribution at each temperature was calculated using the Sjolander [46] formalism and subtracted. In simulations, one can also compute $g^{(n)}(E)$ from the calculated partial phonon DOS, $g_k(E)$, as follows:

$$g^n(E) = B\Sigma_k \left\{ \frac{4\pi b_k^2}{m_k} \right\} g_k(E) \qquad (2)$$

Where B is a normalization constant, m_k, b_k and $g_k(E)$ are the mass, neutron scattering length and partial phonon DOS of kth type of atom, respectively. The weighting factors $\frac{4\pi b_k^2}{m_k}$ for W, Mo, and Se are: 0.025,

0.060, and 0.105 in units of barns/amu, respectively. The neutron scattering lengths for various atoms can be found in Ref [47].

COMPUTATIONAL DETAILS

Ab-initio Molecular dynamics: Ab-initio molecular dynamics simulations were performed within the density functional theory (DFT) framework implemented in the Vienna Ab-initio Simulation Package (VASP)[48, 49]. The simulations used the projector-augmented wave formalism[50] and the generalized gradient approximation exchange-correlation functional parameterization by Perdew, Burke, and Ernzerhof[51, 52]. The DFT-D3 method with Becke-Johnson damping function was used to account for the van der Waals dispersive interactions between WSe_2/$MoSe_2$ layers along the *c*-axis[53, 54]. At ambient conditions, WSe_2 and $MoSe_2$ crystallize in a hexagonal structure (space group no. 194, P63/mmc) that contains six atoms in the unit-cell (2 metal atoms and 4 Se) (**Figure S1[45]**). A $4\times4\times1$ supercell (96 atoms) was used for AIMD simulations. For DFT calculations, we used a $2\times2\times2$ k-point mesh generated using the Monkhorst-Pack method[55], and a plane-wave energy cut-off of 800 eV. Before AIMD simulations, we fully relaxed the crystal structure with an energy and Hellmann-Feynman force convergence thresholds of 10^{-8} eV and 10^{-6} eV/Å, respectively, and obtained the optimized lattice constants *a* and *c* shown in Table S1 [45]. The total energy convergence criteria were set to 10^{-6} eV. The simulations were performed from 100 K to 1000 K in intervals of 100 K within the NVT framework, and the temperatures were controlled using a Nose-Hoover thermostat[55]. All the simulations were run for 10-15 ps with a time step of 2 fs.

Machine Learned Molecular Dynamics (MLMD): The DEEP-MD code was used to generate a machine-learned surrogate force field based on a neural network representation [56]. Subsequent MLMD simulations were performed with this DEEP-MD potential using LAMMPS[57]. The generated force field was tested against several quantities also computed from AIMD (see **Figure S2[45]**). The phonon spectral energy density (SED) was computed based on MLMD on a $20\times20\times10$ supercell (24000 atoms) up to 100 ps, which provides a *Q*- and *E*-resolution of 0.05 *rlu* and 0.05 meV, respectively.

Lattice thermal conductivity from MLMD: To compute the thermal conductivity within the Green-Kubo formalism, we performed MLMD simulations on a $24\times24\times5$ supercell (17280) up to 2 ns with 1 fs time

steps at 100 K, 300 K, 500 K and 700 K for both WSe_2 and $MoSe_2$. The heat-flux vector, $\boldsymbol{J}(t)$ is given by:

$$\boldsymbol{J}(t) = \sum_i \boldsymbol{v}_i \varepsilon_i + \frac{1}{2}\sum_{ij, i \neq j} \boldsymbol{r}_{ij}(\boldsymbol{F}_{ij} \cdot \boldsymbol{v}_i) \qquad (3)$$

where ε_i and $\boldsymbol{v}_i$ are the energy and velocity of the ith particle and $\boldsymbol{F}_{ij}$ is the force between i^{th} and j^{th} atoms. The first and second terms in **equation (3)** represent the convection and conduction terms of heat flux, respectively. Convection results from the mass transport of mobile (diffusive) species, while the second term describes the energy exchange due to interatomic interactions, e.g., lattice vibrations in crystalline solids. In non-diffusive solids, the convection term is insignificant. The total lattice thermal conductivity tensor (κ_l^{uv}) was calculated using the Green-Kubo formalism [39], within which it is expressed as a time integral of the heat current autocorrelation function. In this approach, the lattice thermal conductivity tensor element κ_l^{uv} (u, v=x,y,z) is given by:

$$\kappa_l^{uv} = \frac{1}{k_B T^2 V}\int_0^t <J_u(0)J_v(t)> dt \qquad (4)$$

Where $J_u(t)$ is the heat-flux component along the u direction at time t.

Lattice thermal conductivity simulation from perturbation theory: The lattice thermal conductivity (κ_l) using the perturbation method was calculated using 2nd, 3rd and 4th order force constant using ShengBTE. These force-constants were evaluated at 0 K. To investigate the effect of temperature on force-constants and subsequently on κ_l, we have computed κ_l using 2nd and 3rd-order renormalized force constants (FC) at 300 K implemented in TDEP[58, 59].

The thermal conductivity, κ_l is expressed as:

$$\kappa_l = \frac{1}{3}\sum_\lambda C_{v_\lambda} v_{g_\lambda}^2 \tau_\lambda \qquad (5)$$

where C_{v_λ}, v_{g_λ} and τ_λ are the heat capacity, group velocity, and lifetime, which correspond to a specific phonon mode λ, respectively. λ consists of $\boldsymbol{q}$ and j, which are the phonon wave vector and branch number.

The C_{v_λ} and v_{g_λ} can be determined from harmonic phonons, while τ_λ can be determined by calculating the phonon scattering rate due to three or higher order phonon-phonon scattering as well as from other scattering processes, here, we only consider the phonon-phonon scattering. The harmonic interatomic force constants (IFC) are calculated using a 4 × 4 × 1 supercell and a 2 × 2 × 2 Monkhorst-Pack grid within a finite displacement scheme, as implemented in the open-source software package Phonopy[60]. The third and fourth-order IFCs were calculated through *thirdorder* and *fourthorder* packages of ShengBTE, considering up to the third-nearest neighbours. The same supercell size and k-point mesh were used to calculate the third and fourth IFCs from a finite difference method. With these IFCs, the phonon frequencies and velocities are then obtained by diagonalizing the dynamical matrix, and the three-phonon scattering rates are calculated from the iterative solution of the BTE, while four-phonon scatterings were calculated within relaxation time approximation. The thermal conductivity is solved on a 24 × 24 × 5 q-mesh, sufficient to integrate the BZ (**Figure S3[45]**). The expressions for all involved scattering rates are described in Ref [34, 36].

Spectral energy density (SED): The phonon SED at wavevector $\vec{q}$ and energy E was obtained from MLMD trajectories using the following formalism [61]:

$$\varphi(\vec{q},E) = \frac{1}{4\pi\tau_0 N}\Sigma_{\alpha,k}m_k \left| \Sigma_{n=1}^N \int_0^{\tau_0} \vec{u}_\alpha\binom{n}{k};t\right) \exp\left[i\vec{q}.\vec{r}\binom{n}{k} - iEt/\hbar\right]dt \right|^2 \quad (6)$$

where N is the number of unit cells in a supercell (N= $N_1 \times N_2 \times N_3$), summation index α runs over Cartesian x,y, and z; index k runs over the number of particles in the unit cell. m_k, $\vec{r}\binom{n}{k}$ are the mass of kth atom and its equilibrium position in the nth unit cell, and $\vec{u}_\alpha\binom{n}{k};t$ is the velocity of kth atom in the nth unit cell at time t.

RESULTS AND DISCUSSION

X-ray Diffraction, Inelastic Neutron Scattering and Phonons Dynamics

We have performed the temperature-dependent X-ray diffraction measurements on polycrystalline samples of $MoSe_2$ and WSe_2 from 20 K to 280 K, as shown in **Figure 1**. There are no impurity peaks in the XRD pattern, confirming the single-phase nature of the sample. The XRD peaks are indexed as per

the data reported in Powder Diffraction File ICDD JCPDS-PDF 04-004-8782 and 00-038-1388 for hexagonal (space group P63/mmc) MoSe2 and WSe2, respectively.

The INS measurements were carried out at five temperatures: 313 K, 498 K, 673 K, 898 K, and 1098 K (**Figure 2** and **Figure S4[45]**). The phonon spectra of $MoSe_2$ and WSe_2 extend up to 45 and 40 meV, respectively. The temperature-dependent spectra show several peaks around 5, 14, 16, 19, 22, 26, and 36 in $MoSe_2$ and 5, 13, 15,24, 27 and 32 meV in WSe_2. From our partial DOS calculations, we found that the entire spectral range (0 - 45 meV) is contributed by both Mo/W and Se dynamics. Interestingly, even at 1098 K, the low-E (< 10 meV) phonon spectra do not show any significant change, while above 10 meV, the phonon peaks clearly soften. The low-E portion of the spectra is largely attributed to phonons from acoustic branches and the three lowest optical branches. The softening and broadening of phonon modes are attributed to lattice expansion (implicit anharmonicity) and phonon-phonon interactions (explicit anharmonicity). The implicit anharmonic shifts largely contribute to the thermal expansion, while the explicit anharmonicity dominates thermal transport. Hence, we have computed both anharmonic components in the entire BZ to identify the modes relevant to thermal expansion and lattice thermal conductivity.

We performed NVT-MLMD simulation to explicitly probe the temperature evolution of the neutron-weighted phonon spectra (**Figure 2(b, e)**). We observe that the simulated low-E modes do not show significant change with temperature, while the high energy modes slightly soften at elevated temperatures as experimentally observed, although less in magnitude than in the measured spectra. The AIMD simulated phonon DOS as a function of temperatures are also shown in **Figure S7**.

To further probe the temperature behaviour of low-E modes, we plot the measured Q-integrated dynamical structure factor, $S(E)$ (1.0 Å^{-1} <Q< 4.0 Å^{-1}) in **Figure 2(c,f)**. This plot clearly shows that the modes barely shift on warming but do visibly broaden. We expect the explicit anharmonicity due to the phonon-phonon interactions and increased phonon amplitudes, and the implicit anharmonicity due to the volume changes. Our detailed calculations show that the negligible shift of the low-E modes occurs due a cancellation of the hardening due to the fourth and higher order explicit anharmonicity and the softening due the implicit anharmonicity of these modes.

To investigate the effect of third-order and higher-order anharmonicity on phonon spectra, we computed the phonon spectral energy density (SED) along various high-symmetry directions in the Brillouin zone (BZ) using two different approaches. The first approach is based on the TDEP method, which computes the phonon SED using third-order force-constants only (referred to here as TDEP-SED),

and the second approach is based on molecular dynamics trajectories (NVT-MLMD) [61] and referred to here as MLMD-SED. The latter approach includes third and higher-order anharmonicity to phonon SED. Hence, comparing the phonon SED from the two methods helps us identify the region in the BZ dominated by fourth or higher-order anharmonicity. In **Figure 3**, we plot the TDEP-SED and MLMD-SED at 100 K and 500K. The TDEP-SED at 100 K shows sharp features in intensity profiles and does not change significantly at 500 K in both compounds. However, while the MLMD-SED also shows sharp phonon peaks at 100 K, these become significantly broader at 500 K, making the MLMD-SED look more diffuse compared to the TDEP-SED.

Lattice Thermal Conductivity and anharmonic phonons

In the harmonic picture of lattice dynamics, the phonons are non-interacting and infinitely long-lived quasiparticles and hence an infinite lattice thermal conductivity. However, phonons in real systems get scattered by other phonons (intrinsic scattering processes), leading to a finite lifetime of phonons. Crystal defects and finite sample size further reduce the phonon lifetimes, and the shortened mean free paths limit the phononic thermal conductivity (extrinsic scattering processes). In ideal single-crystals, the finite lattice thermal conductivity results from intrinsic phonon scattering processes, namely Umklapp and normal processes. Generally, the normal processes do not directly contribute to the thermal resistance. The Umklapp processes are the leading phonon scattering processes in heat conduction at high temperatures. Further, the intrinsic phonon scattering processes may involve three or more phonons. Three-phonon scattering processes include two phonons annihilating and creating a new phonon or one phonon splitting into two phonons. This is generally the dominant scattering channel in crystalline materials and leads to $1/T$ dependence of κ_l. However, some materials such as BAs, perovskites, Heusler alloys (and others)[62-70] show limited scattering space for three phonon processes and significantly higher scattering phase space for four phonon processes, and as a result do not exhibit the typical $1/T$ dependence of κ_l, with a lower conductivity than three-phonon processes alone.

From INS measurements and MLMD simulations, we find that the phonons in both compounds do not change significantly at elevated temperatures; hence phase space and group velocity would not show any significant change. However, phonons substantially broaden on heating, corresponding to decreased lifetimes. The temperature dependence of thermal conductivity in these compounds is therefore primarily governed by phonon lifetimes. We first calculated the lattice thermal conductivity using third-

order force constants at 0 K using ShengBTE (κ^{Sheng3}). In this approach, the phonon lifetime is only contributed by three-phonon scattering processes. In **Figure 4(a-b) and Figure S5**, we have shown the three-phonon scattering rates, life times and group velocities in $MoSe_2$ and WSe_2 at 300 K. The lattice thermal conductivity in $MoSe_2$ and WSe_2 was measured by Puqing Jiang *et al.* [23] using a time-domain thermoreflectance approach and found large anisotropy between the in-plane and out-of-plane lattice thermal conductivity. In **Figure 4(c-f)**, we have shown the calculated thermal conductivity from three phonon processes in ab-plane and along the *c*-axis, and also shown the experimental values[23]. However, three-phonon scattering has shown a significant overestimation of thermal conductivity compared to experimental values ($\kappa^{\text{Expt.}}$). Including the four-phonon scattering rates improves this discrepancy, and we examined their impact on the thermal conductivity and phonon lifetimes using ShengBTE (κ^{Sheng4}). Here also, the fourth-order force constants were evaluated at 0 K. We found that four-phonon scattering resistance significantly reduces the thermal conductivities and phonon lifetimes but is still overestimated compared to experimental values (**Figure 4**). This suggests that either higher-order processes dominate and/or that the third and fourth-order force constants at 0 K are insufficient. To further probe these aspects, we also used the renormalized second and third-order force constants to compute the thermal conductivity at respective temperatures using TDEP (κ^{TDEP}). Surprisingly, we find that the κ^{TDEP} at low-*T* shows lower thermal conductivity values than κ^{Sheng4}; however, they are nearly the same at higher temperatures (**Figure 4**). This indicates that the 0 K anharmonic force constants cannot explain the measured thermal conductivity, and one also needs to consider the temperature dependence of higher-order force-constants. However, it is currently not feasible to evaluate the temperature dependence of forth-order force constants and their effect on thermal conductivity due to TDEP limitations.

To further analyze the full impact of anharmonicity on κ, we performed MLMD simulations and, evaluated the thermal conductivity within the Green-Kubo formalism, κ^{GK}. Strikingly, the κ^{GK} from MLMD reproduces the measured in-plane thermal conductivity (κ_{xy}^{expt}) very well and over a wide range of temperatures. However, the out-of-plane component (κ_z^{expt}) is somewhat overestimated. It is important to note that these TMDCs have a weak interplanar interaction and are governed by van der Waals forces. In the DFT framework, precisely capturing the van der Waals interactions is difficult and may lead to an overestimated thermal conductivity along the c-axis. Hence, the extensive simulation based on the perturbation method and MLMD Green-Kubo approach indicates that the importance of temperature effect on higher-order force-constants is critical in understanding and predicting the thermal conductivity. To determine which phonon modes are most critical in heat transport in the ab-plane and along the c-axis,

we computed the mode-resolved in-plane and out-of-plane lattice thermal conductivity as a function of phonon energy at 300 K (**Figure 5**). Interestingly, more than 90% of lattice thermal conductivity is attributed to modes below 20 meV. By comparing the different methods, it appears that the higher-order scattering processes and temperature-renormalised force constants are critical for precisely evaluating these low-*E* phonon lifetimes and, hence, the thermal conductivity of TMDCs. The effect of higher-ordered scattering processes and their temperature dependence was also observed in strongly anharmonic superionics and 2-d materials, including WS_2 and graphene, where the impact of higher-order anharmonicity on thermal conductivity is found to be significant [71-79].

Lattice thermal expansion behaviour and phonon anharmonicity

Thermal expansion is also associated with anharmonicity in the potential energy surface. Knowing the phonon frequency shifts with temperature and volume, one can estimate how the material would behave at a given temperature. The phonon frequency shifts due to change in the vibrational amplitudes with temperature are usually much smaller than the frequency shifts due to the change in volume with temperature[32]. We have calculated the phonon frequencies at different volumes using lattice dynamics within the quasi-harmonic approximation (QHA).

In the quasi-harmonic approximation, the volume thermal expansion coefficient [42] of a crystalline material is given by the following relation: $\alpha_V = \frac{1}{BV}\sum_i \Gamma_i C_{Vi}(T)$. Here $\Gamma_i = -\frac{V}{E_i}\frac{dE_i}{dV}$ is the mode Grüneisen parameter, which is a measure of pressure response of the phonon energy to determine the nature of the expansion behaviour. For instance, the phonon modes with negative values of Γ tend to contract the lattice, while the positive ones would expand the lattice. $C_{Vi}(T)$ is the specific heat contribution of the ith phonon mode (of energy E_i) at temperature T, while B and V stand for the bulk modulus and volume of the compound, respectively. The calculated elastic constants and bulk modulus are given in **TABLE S2** [45]. The pressure dependence of the phonon spectra within QHA has been calculated in the entire Brillouin zone to allow for the calculation of the energy dependence of the Grüneisen parameter $\Gamma(E)$ and further processed to obtain the thermal expansion coefficient $\alpha_V(T)$.

The volume dependence of the phonon spectra within QHA has been calculated in the entire Brillouin zone to allow for the calculation of the mode-wise Grüneisen parameter $\Gamma(qj, E)$ (**Figure 4(e,f)**)

and to obtain the thermal expansion coefficient $\alpha_V(T)$. We have calculated the mode-wise thermal expansion contribution on a $20\times20\times10$ q-point grid in the BZ at 300 K, as shown in **Figure S6**[45]. It is evident that the most significant contribution to thermal expansion comes from low-E modes. We have performed temperature-dependent X-ray diffraction measurements on $MoSe_2$ and WSe_2 from 50 K to 300 K. The temperature dependence of fractional change in volume with respect to 50 K is shown in **Figure 5(e, f)**, which exhibits positive expansion. The large implicit anharmonicity of the low-E modes leads to large thermal expansion. It is interesting to note that the same low-E modes exhibit rather small explicit anharmonicity and contribute most to thermal conductivity.

CONCLUSIONS

We combined inelastic neutron scattering measurements, ab-initio and machine-learned molecular dynamics simulations to unravel the phonon anharmonicity and their role in thermal transport and thermal expansion in $MoSe_2$ and WSe_2. We find that low-energy phonons play a crucial role in determining both the thermal-expansion behaviour and heat transport in these materials. Conventional perturbation methods are insufficient to capture the temperature-dependent anharmonicity of these phonon modes, particularly the low-E modes in strongly anharmonic systems. Machine-learned molecular dynamics simulations pave the way to completely treat the anharmonicity of phonons by performing temperature-dependent large-scale molecular dynamics simulations. These results establish the importance of anharmonic low-energy modes in TMDCs, which drive the thermal and transport properties.

1. S. Manzeli, D. Ovchinnikov, D. Pasquier, O. V. Yazyev and A. Kis, *Nature Reviews Materials*, 2017, **2**, 17033.
2. B. Radisavljevic, A. Radenovic, J. Brivio, V. Giacometti and A. Kis, *Nature Nanotechnology*, 2011, **6**, 147-150.
3. Q. H. Wang, K. Kalantar-Zadeh, A. Kis, J. N. Coleman and M. S. Strano, *Nature Nanotechnology*, 2012, **7**, 699-712.
4. X. Hong, J. Kim, S.-F. Shi, Y. Zhang, C. Jin, Y. Sun, S. Tongay, J. Wu, Y. Zhang and F. Wang, *Nature Nanotechnology*, 2014, **9**, 682-686.
5. M. Massicotte, P. Schmidt, F. Vialla, K. G. Schädler, A. Reserbat-Plantey, K. Watanabe, T. Taniguchi, K. J. Tielrooij and F. H. L. Koppens, *Nature Nanotechnology*, 2016, **11**, 42-46.
6. H. Liang, Z. Cao, F. Ming, W. Zhang, D. H. Anjum, Y. Cui, L. Cavallo and H. N. Alshareef, *Nano Letters*, 2019, **19**, 3199-3206.
7. K. Nassiri Nazif, A. Daus, J. Hong, N. Lee, S. Vaziri, A. Kumar, F. Nitta, M. E. Chen, S. Kananian, R. Islam, K.-H. Kim, J.-H. Park, A. S. Y. Poon, M. L. Brongersma, E. Pop and K. C. Saraswat, *Nature Communications*, 2021, **12**, 7034.
8. D. B. Velusamy, R. H. Kim, S. Cha, J. Huh, R. Khazaeinezhad, S. H. Kassani, G. Song, S. M. Cho, S. H. Cho, I. Hwang, J. Lee, K. Oh, H. Choi and C. Park, *Nature Communications*, 2015, **6**, 8063.
9. W. Huang, H. Da and G. Liang, *Journal of Applied Physics*, 2013, **113**, 104304.
10. S. Kumar and U. Schwingenschlögl, *Chemistry of Materials*, 2015, **27**, 1278-1284.
11. H.-P. Komsa, J. Kotakoski, S. Kurasch, O. Lehtinen, U. Kaiser and A. V. Krasheninnikov, *Physical Review Letters*, 2012, **109**, 035503.
12. G. Wang, C. Robert, M. M. Glazov, F. Cadiz, E. Courtade, T. Amand, D. Lagarde, T. Taniguchi, K. Watanabe, B. Urbaszek and X. Marie, *Physical Review Letters*, 2017, **119**, 047401.
13. F. Wu, T. Lovorn, E. Tutuc, I. Martin and A. H. MacDonald, *Physical Review Letters*, 2019, **122**, 086402.
14. D. Li, H. Shan, C. Rupprecht, H. Knopf, K. Watanabe, T. Taniguchi, Y. Qin, S. Tongay, M. Nuß, S. Schröder, F. Eilenberger, S. Höfling, C. Schneider and T. Brixner, *Physical Review Letters*, 2022, **128**, 087401.
15. Z. Lin, Y. Liu, Z. Wang, S. Xu, S. Chen, W. Duan and B. Monserrat, *Physical Review Letters*, 2022, **129**, 027401.
16. Y.-M. Wu, Z. Wu and H. Yao, *Physical Review Letters*, 2023, **130**, 126001.
17. H. Guo, T. Yang, P. Tao, Y. Wang and Z. Zhang, *Journal of Applied Physics*, 2013, **113**, 013709.
18. D. Sarkar, W. Liu, X. Xie, A. C. Anselmo, S. Mitragotri and K. Banerjee, *ACS Nano*, 2014, **8**, 3992-4003.
19. C. Chiritescu, D. G. Cahill, N. Nguyen, D. Johnson, A. Bodapati, P. Keblinski and P. Zschack, *Science*, 2007, **315**, 351-353.
20. S. Manzeli, D. Dumcenco, G. Migliato Marega and A. Kis, *Nature Communications*, 2019, **10**, 4831.
21. L. Gao, *Small*, 2017, **13**, 1603994.
22. W. Choi, N. Choudhary, G. H. Han, J. Park, D. Akinwande and Y. H. Lee, *Materials Today*, 2017, **20**, 116-130.
23. P. Jiang, X. Qian, X. Gu and R. Yang, *Advanced Materials*, 2017, **29**, 1701068.
24. D. O. Lindroth and P. Erhart, *Physical Review B*, 2016, **94**, 115205.
25. J. J. Bae, H. Y. Jeong, G. H. Han, J. Kim, H. Kim, M. S. Kim, B. H. Moon, S. C. Lim and Y. H. Lee, *Nanoscale*, 2017, **9**, 2541-2547.
26. X. Gu, B. Li and R. Yang, *Journal of Applied Physics*, 2016, **119**, 085106.
27. R. Yan, J. R. Simpson, S. Bertolazzi, J. Brivio, M. Watson, X. Wu, A. Kis, T. Luo, A. R. Hight Walker and H. G. Xing, *ACS Nano*, 2014, **8**, 986-993.

28. J. Judek, A. P. Gertych, M. Świniarski, A. Łapińska, A. Dużyńska and M. Zdrojek, *Scientific Reports*, 2015, **5**, 12422.
29. X. Zhang, D. Sun, Y. Li, G.-H. Lee, X. Cui, D. Chenet, Y. You, T. F. Heinz and J. C. Hone, *ACS Applied Materials & Interfaces*, 2015, **7**, 25923-25929.
30. I. Jo, M. T. Pettes, E. Ou, W. Wu and L. Shi, *Applied Physics Letters*, 2014, **104**, 201902.
31. V. A. Drebushchak, *Journal of Thermal Analysis and Calorimetry*, 2020, **142**, 1097-1113.
32. R. Mittal, M. K. Gupta and S. L. Chaplot, *Progress in Materials Science*, 2018, **92**, 360-445.
33. X. Qian, J. Zhou and G. Chen, *Nature Materials*, 2021, **20**, 1188-1202.
34. Z. Han, X. Yang, W. Li, T. Feng and X. Ruan, *Computer Physics Communications*, 2022, **270**, 108179.
35. A. Togo, L. Chaput and I. Tanaka, *Physical Review B*, 2015, **91**, 094306.
36. W. Li, J. Carrete, N. A. Katcho and N. Mingo, *Computer Physics Communications*, 2014, **185**, 1747-1758.
37. A. J. McGaughey and M. Kaviany, *Advances in heat transfer*, 2006, **39**, 169-255.
38. M. S. Green, *The Journal of Chemical Physics*, 1954, **22**, 398-413.
39. R. Kubo, *Reports on progress in physics*, 1966, **29**, 255.
40. R. Kubo, M. Yokota and S. Nakajima, *Journal of the Physical Society of Japan*, 1957, **12**, 1203-1211.
41. F. Müller-Plathe, *The Journal of Chemical Physics*, 1997, **106**, 6082-6085.
42. Z. Fan, H. Dong, A. Harju and T. Ala-Nissila, *Physical Review B*, 2019, **99**, 064308.
43. J.-S. Wang, J. Wang and N. Zeng, *Physical Review B*, 2006, **74**, 033408.
44. N. Mingo and L. Yang, *Physical Review B*, 2003, **68**, 245406.
45. *See Supplementary Material for forec-field validation, Sample Preparation, numerical data of thermal conductivities, phonon DOS, group velocity and lifetime calculations.*
46. A. Sjolander, *arkiv für Fysik* 1958, **14**.
47. D. Price and K. Skold, *Journal*, 1986.
48. G. Kresse and J. Furthmüller, *Physical Review B*, 1996, **54**, 11169.
49. G. Kresse and J. Furthmüller, *Computational materials science*, 1996, **6**, 15-50.
50. G. Kresse and D. Joubert, *Physical Review B*, 1999, **59**, 1758.
51. J. Perdew, K. Burke and M. Ernzerhof, *Physical Review Letters*, 1998, **80**, 891.
52. J. P. Perdew, K. Burke and M. Ernzerhof, *Physical Review Letters*, 1996, **77**, 3865.
53. S. Grimme, J. Antony, S. Ehrlich and H. Krieg, *The Journal of Chemical Physics*, 2010, **132**, 154104.
54. S. Grimme, S. Ehrlich and L. Goerigk, *Journal of Computational Chemistry*, 2011, **32**, 1456-1465.
55. H. J. Monkhorst and J. D. Pack, *Physical Review B*, 1976, **13**, 5188.
56. H. Wang, L. Zhang, J. Han and E. Weinan, *Computer Physics Communications*, 2018, **228**, 178-184.
57. S. Plimpton, *Journal of Computational Physics*, 1995, **117**, 1-19.
58. O. Hellman, P. Steneteg, I. A. Abrikosov and S. I. Simak, *Physical Review B*, 2013, **87**, 104111.
59. O. Hellman and I. A. Abrikosov, *Physical Review B*, 2013, **88**, 144301.
60. A. Togo and I. Tanaka, *Scripta Materialia*, 2015, **108**, 1-5.
61. J. A. Thomas, J. E. Turney, R. M. Iutzi, C. H. Amon and A. J. McGaughey, *Physical Review B*, 2010, **81**, 081411.
62. T. Yue, Y. Zhao, J. Ni, S. Meng and Z. Dai, *npj Computational Materials*, 2023, **9**, 17.
63. Y. Xiao, Y. Zhao, J. Ni, S. Meng and Z. Dai, *Materials Today Communications*, 2023, **35**, 105450.
64. X. Song, J. Wang, Y. Zhao, J. Ni, S. Meng and Z. Dai, *Physics Letters A*, 2022, **456**, 128550.
65. Y. Zhao, S. Zeng, G. Li, C. Lian, Z. Dai, S. Meng and J. Ni, *Physical Review B*, 2021, **104**, 224304.

66. C. Zhang, J. Sun, Y. Shen, W. Kang and Q. Wang, *The Journal of Physical Chemistry Letters*, 2022, **13**, 5734-5741.
67. T. Feng, L. Lindsay and X. Ruan, *Physical Review B*, 2017, **96**, 161201.
68. K.-C. Zhang, C. Shen, H.-B. Zhang, Y.-F. Li and Y. Liu, *Physical Review B*, 2022, **106**, 235202.
69. N. K. Ravichandran and D. Broido, *Physical Review X*, 2020, **10**, 021063.
70. F. Tian, B. Song, X. Chen, N. K. Ravichandran, Y. Lv, K. Chen, S. Sullivan, J. Kim, Y. Zhou, T.-H. Liu, M. Goni, Z. Ding, J. Sun, G. A. G. Udalamatta Gamage, H. Sun, H. Ziyaee, S. Huyan, L. Deng, J. Zhou, A. J. Schmidt, S. Chen, C.-W. Chu, P. Y. Huang, D. Broido, L. Shi, G. Chen and Z. Ren, *Science*, 2018, **361**, 582-585.
71. A. She, Y. Zhao, J. Ni, S. Meng and Z. Dai, *International Journal of Heat and Mass Transfer*, 2023, **209**, 124132.
72. G. Sun, J. Ma, C. Liu, Z. Xiang, D. Xu, T.-H. Liu and X. Luo, *International Journal of Heat and Mass Transfer*, 2023, **215**, 124475.
73. G.-H. Liu, Z.-X. Xie, P.-Z. Jia, X.-J. Wu and X.-K. Chen, *Diamond and Related Materials*, 2023, **137**, 110116.
74. G. Zhang, S. Dong, C. Yang, D. Han, G. Xin and X. Wang, *Applied Physics Letters*, 2023, **123**.
75. J. Tang, G. Li, Q. Wang, J. Zheng, L. Cheng and R. Guo, *International Journal of Heat and Mass Transfer*, 2023, **207**.
76. J. Han, Q. Zeng, K. Chen, X. Yu and J. Dai, *Nanomaterials*, 2023, **13**.
77. Q. Ren, M. K. Gupta, M. Jin, J. Ding, J. Wu, Z. Chen, S. Lin, O. Fabelo, J. A. Rodríguez-Velamazán, M. Kofu, K. Nakajima, M. Wolf, F. Zhu, J. Wang, Z. Cheng, G. Wang, X. Tong, Y. Pei, O. Delaire and J. Ma, *Nature Materials*, 2023, DOI: 10.1038/s41563-023-01560-x.
78. M. K. Gupta, J. Ding, D. Bansal, D. L. Abernathy, G. Ehlers, N. C. Osti, W. G. Zeier and O. Delaire, *Advanced Energy Materials*, 2022, **12**, 2200596.
79. M. K. Gupta, J. Ding, N. C. Osti, D. L. Abernathy, W. Arnold, H. Wang, Z. Hood and O. Delaire, *Energy & Environmental Science*, 2021, **14**, 6554-6563.
80. Q. Cai, B. Wei, Q. Sun, A. H. Said and C. Li, *Materials Today Physics*, 2022, **28**, 100856.

Figure 1: The temperature dependence of XRD pattern of MoSe$_2$ (ICDD JCPDS-PDF 04-004-8782) and WSe$_2$ (ICDD JCPDS-PDF 00-038-1388). All the peaks are indexed using hexagonal symmetry with space group P6$_3$/mmc.
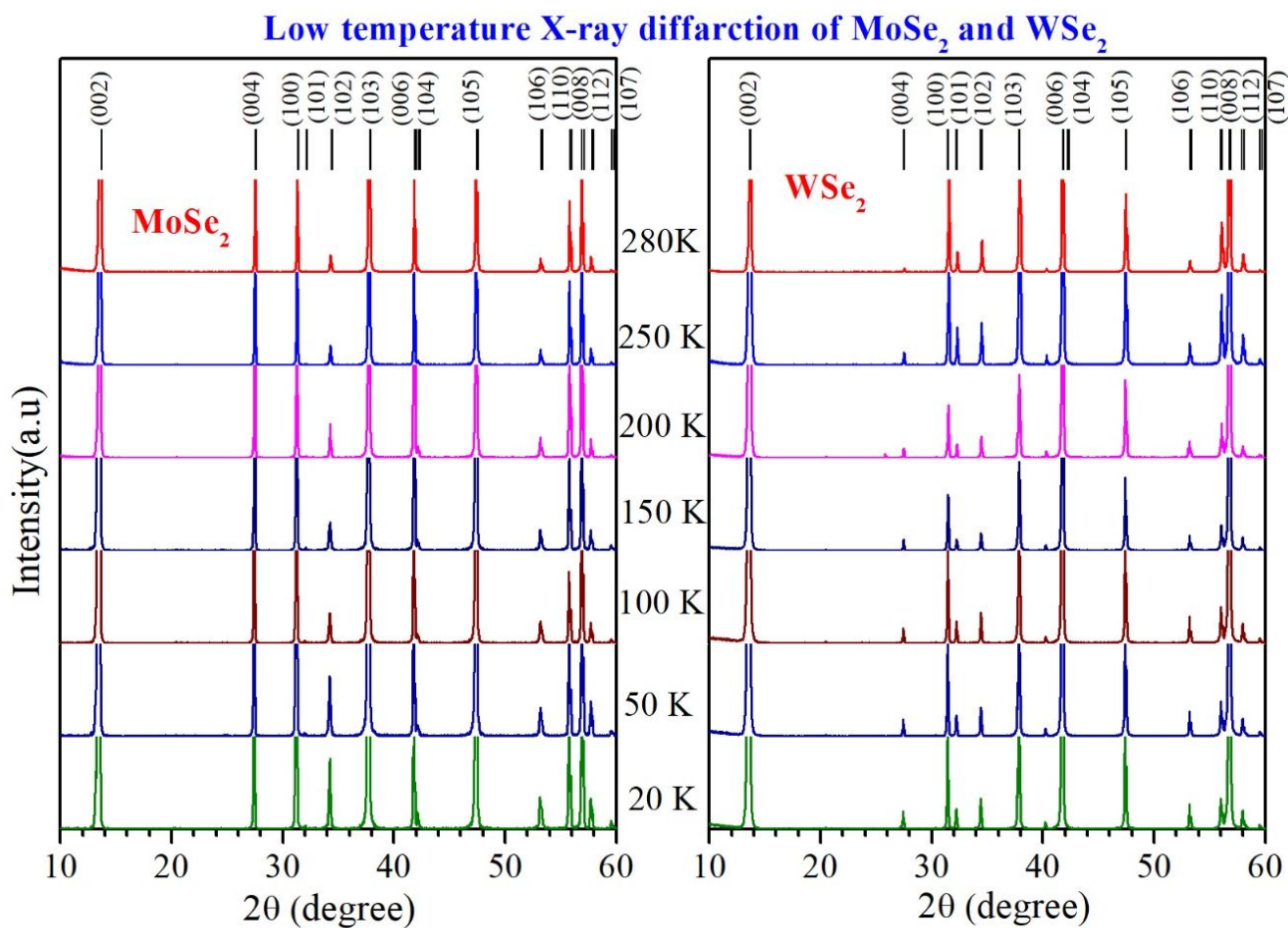
Figure2. (a, d) Temperature dependence of the measured neutron-weighted PDOS $g^{(n)}(E)$ of MoSe$_2$ and WSe$_2$; (b, e) MLMD simulations of $g^{(n)}(E)$ of MoSe$_2$ and WSe$_2$; (c,f) The low-energy part of S(E) spectra of MoSe$_2$ and WSe$_2$ measured with INS, with the simulated S(E) shown in inset.
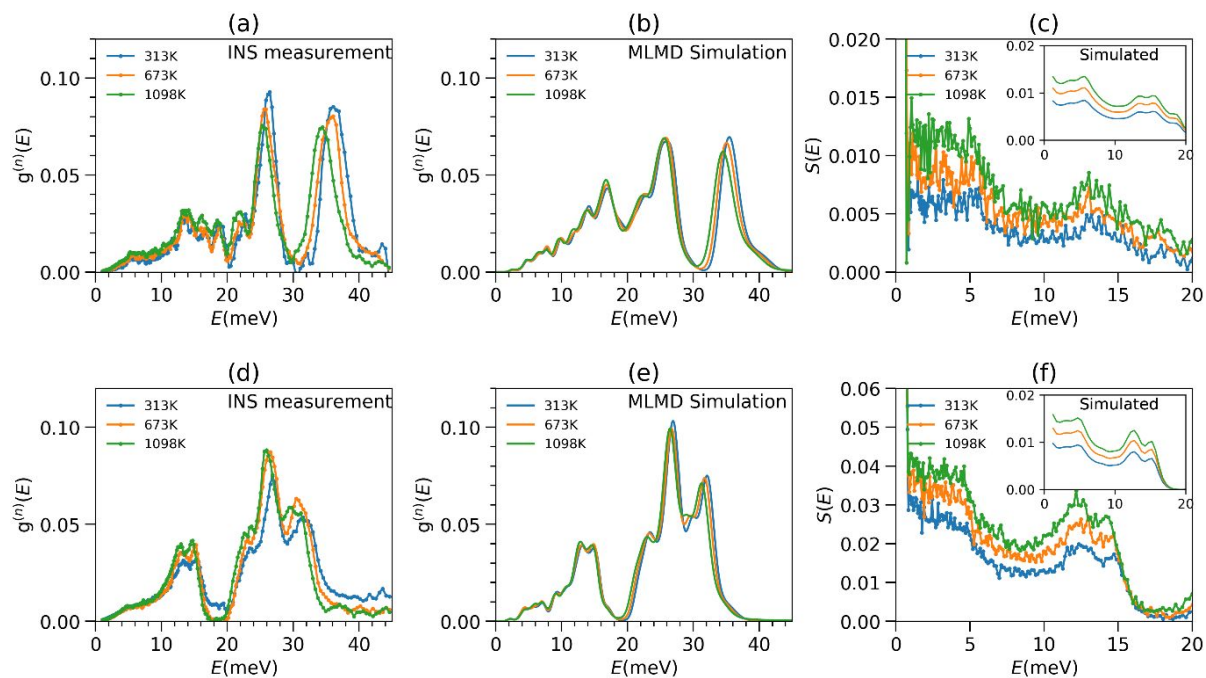

17

Figure 3. (Top panel) The TDEP-calculated phonon SED (including up to third-order anharmonicity) at 100 K and 500 K in $MoSe_2$ and WSe_2. (Bottom-panel) The MLMD-calculated phonon SED (including all orders of anharmonicity) at 100K and 500 K in $MoSe_2$ and WSe_2. The red markers in WSe_2 SED are the phonon energies measured at 300 K by Cai *et al.* [80].
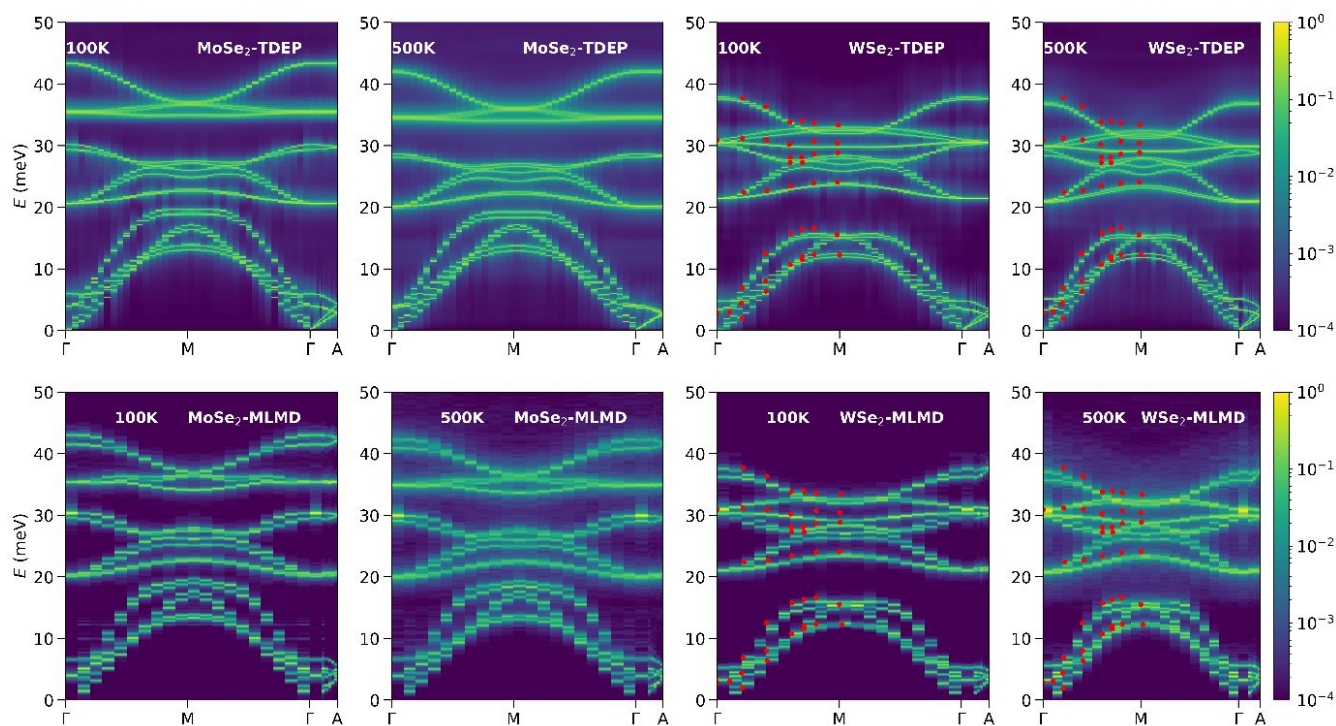
Figure 4. (a, b) Calculated mode-resolved phonon scattering rates on a (24x24x7) q-point grid in BZ in MoSe$_2$ and WSe$_2$ at 300 K using 3-phonon scattering, calculated from 2nd and 3rd-order force-constants at 0 K (ShengBTE-3ph), and renormalized 2nd and 3rd-order force-constants at 300 K (TDEP-3ph). The scattering rates are also calculated using 3- and 4- phonon scattering processes using 0 K 3rd and 4th order force-constants (ShengBTE 3ph+4ph). (c,d) The calculated in-plane lattice thermal conductivity (κ_{xy}) and (e, f) out-of-plane lattice thermal conductivity (κ_z), using 3-phonon scattering from ShengBTE-3ph, TDEP-3ph and ShengBTE 3ph+4ph methods and the Green-Kubo method based on equilibrium molecular dynamics simulation, includes all order of anharmonicity. The calculated quantities are compared with available experimental measurements [23]. The numerical values of thermal conductivity from different methods (contribution of 4th and higher order interactions) are given in Table S3.
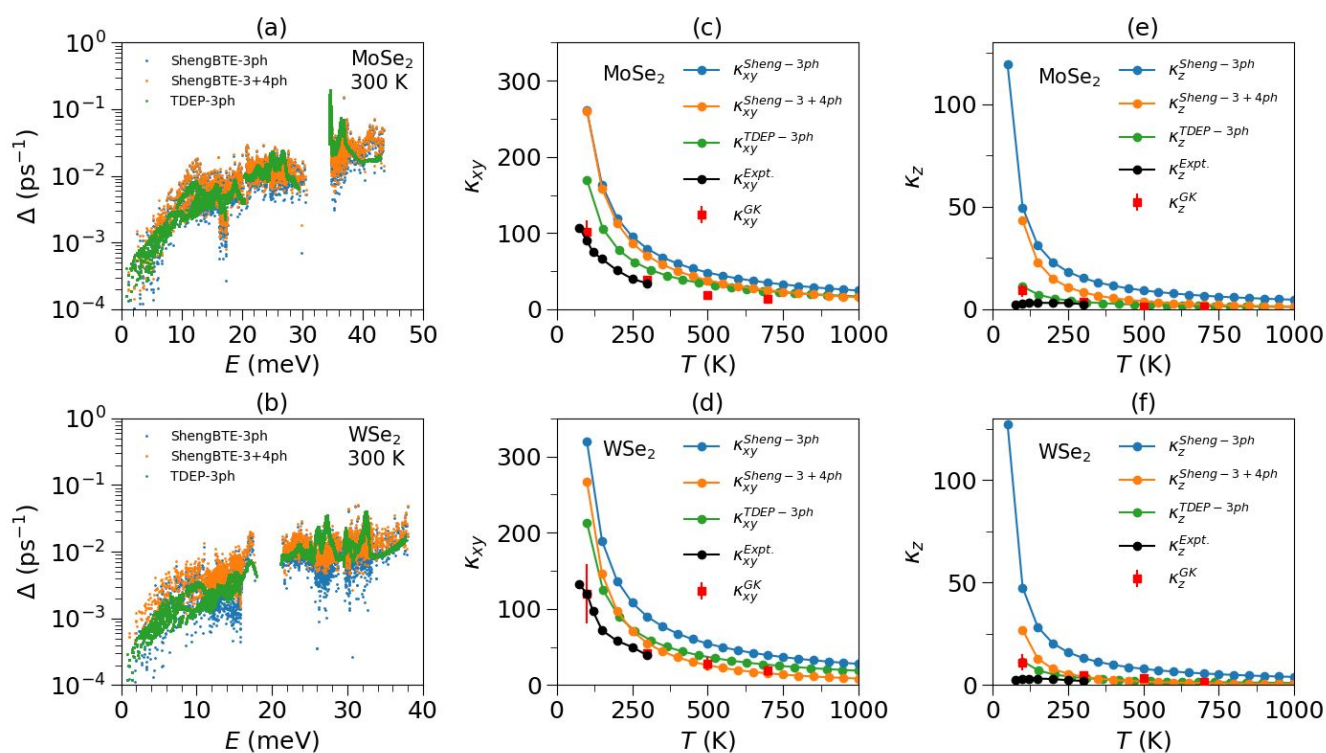
Figure 5. (a, b) The calculated in-plane (κ_{xy}) and (c-d) out-of-plane (κ_z) lattice thermal conductivity contributed from individual modes in BZ (on a 24x24x5 grid) in MoSe$_2$ and WSe$_2$ using (i) 3-phonon processes (lowest order perturbation method) at 0 K (Sheng-BTE 3ph), (ii) 3 and 4 phonon processes at 0 K (Sheng-BTE 3+4ph) and (iii) 3-phonon processes with renormalized force constant at 300 K (TDEP 3ph). (e, f) The calculated mode Grüneisen parameters in MoSe$_2$ and WSe$_2$ using pressure dependence of phonon frequencies, inset shows the fractional change in volume with temperature calculated within QHA and compared with our X-ray measurements.